Article

Development of Bronze Phase Titanium Dioxide Nanorods for Use as Fast-Charging Anode Materials in Lithium-Ion Batteries

Korawith Pimta,[#] Thanapat Autthawong,[#] Waewwow Yodying, Chitsanupong Phromma, Mitsutaka Haruta, Hiroki Kurata, Thapanee Sarakonsri, and Yothin Chimupala*

Read Online

ACCESS | Metrics & More | Article Recommendations | Supporting Information

ABSTRACT: Bronze phase titanium dioxide ($TiO_2(B)$) nanorods were successfully prepared via a hydrothermal method together with an ion exchange process and calcination by using anatase titanium dioxide precursors in the alkali hydrothermal system. TiO_2 precursors promoted the elongation of nanorod morphology. The different hydrothermal temperatures and reaction times demonstrated that the synthesis parameters had a significant influence on phase formation and physical morphologies during the fabrication process. The effects of the synthesis conditions on the tailoring of the crystal morphology were discussed. The growth direction of the $TiO_2(B)$ nanorods was investigated by X-ray diffractometry (XRD) and scanning electron microscopy (SEM). The as-synthesized $TiO_2(B)$ nanorods obtained after calcination were used as anode materials and tested the efficiency of Li-ion batteries. This research will study the effects of particle morphologies and crystallinity of $TiO_2(B)$ derived from a modified hydrothermal method on the capacity and charging rate of the Li-ion battery. The $TiO_2(B)$ nanorods, which were synthesized by using a hydrothermal temperature of 220 °C for 12 h, presented excellent electrochemical performance with the highest Li storage capacity (348.8 mAh/g for 100 cycles at a current density of 100 mA/g) and excellent high-rate cycling capability (a specific capacity of 207.3 mAh/g for 1000 cycles at a rate of 5000 mA/g).

INTRODUCTION

Nowadays, the demand for using new technological innovations is increasing because most people desire a comfortable life, simplicity of motion, and more safety in everyday life. Recently, portable electronic devices, such as mobile phones, headphones, laptops, smartwatches, and electronic tablets, including electric vehicles (EV), medical devices, power tools, and communication tools, have increasingly been brought into everyday life. These applications require energy storage to operate electronic systems.[1] Rechargeable batteries, such as lithium-ion batteries (LIBs), are one of the most effective energy storage systems and have attracted the attention of researchers and industries because the LIBs have high energy density, high specific capacity, long shelf life, long life cycle, low self-discharge rate, no memory effect, and flexible and lightweight design.[1−4] However, the development of high-efficiency LIBs is still essential for the advanced electric vehicle industry. There are also efforts to

bring this battery to other uses, such as aerospace, military, and public utility. For this reason, research related to improving the performance of components in LIBs has received much attention. One of them is the development of anode materials in LIBs. The commercial anode material in LIBs, which is widely used at present, is graphite. Graphite is classified as intercalation/de-intercalation anode material in LIBs, but the disadvantage of graphite is that it has a low operating voltage (0.05 V vs Li/Li^+) and can cause pulverization of materials, which leads to a short circuit and thermal runaway conditions

resulting in the combustion of organic electrolytes and a catastrophic battery explosion.[1,5] Therefore, several researchers are looking for new anode materials to replace graphite.

Recently, titanium dioxide (TiO_2) has been remarkable for use as an anode material in LIBs due to its high structural stability, which contributes to small volume change during the charge−discharge process (~4%), stable capacity retention, and fast charge ability for lithium-ion (Li^+) insertion and desertion.[6] Moreover, TiO_2 has a high operating voltage (1.5−1.7 V vs Li/Li^+), which can prevent the formation of lithium dendrites during cycling. As a result, this anode material avoids short circuit and battery explosion problems, including low cost and environmental friendliness.[6,7] Typically, many TiO_2 polymorphs were selected for use as anode materials in LIBs, namely, anatase, brookite, rutile, and bronze. Hence, the development trend of the TiO_2 anode material in LIBs is interesting, specifically bronze phase titanium dioxide ($TiO_2(B)$) because $TiO_2(B)$ has a unique monoclinic crystal structure and the lowest density (3.73 g/cm^3). Furthermore, $TiO_2(B)$ has channels and voids in the crystal framework that are larger than those in the anatase and rutile phases; as a result, it reduces the volume change problem during Li^+ insertion and extraction processes,[6,8] which extend the cycle life of LIBs and allow for more utilization. In addition, the monoclinic structure of $TiO_2(B)$ can generate the pseudocapacitive behavior in fast lithium storage and transfer (fast charge ability) during charge and discharge in LIBs.[9]

Intercalation-type anode materials,[10] composed of carbonaceous materials (graphite,[11] carbon nanoparticles,[12] porous carbon,[10] graphene,[13] graphene oxide,[14] etc.) and titanium oxides ($Li_4Ti_5O_{12}$,[15] TiO_2,[16] etc.), were compared with $TiO_2(B)$ in the literature, as illustrated in Table S1. It was found that carbon-based materials have a specific capacity close to $TiO_2(B)$ (theoretical specific capacity 335 mAh/g)[17,18] including graphene, which has two faces on the 2-dimensional carbon sheets. However, graphene has some disadvantages. First, graphene has a low density, which reduces its volumetric capacity. Re-stacking of graphene sheets may cause the loss of their unique strengths. In addition, the synthesis of enormous surface area and highly conductive graphene is difficult, and controlling impurities/defects on graphene sheets is sophisticated.[17,19] Furthermore, the redox potentials versus Li/Li^+ of carbon-based materials are lower than $TiO_2(B)$, which makes using carbon-based materials in LIBs more likely to cause dendritic lithium during the charging and discharging process, causing an internal short circuit, than using the $TiO_2(B)$ anode material in LIBs.[20] In the case of titanium oxides, the theoretical specific capacity of $TiO_2(B)$ was higher than that of $Li_4Ti_5O_{12}$ (175 mAh/g),[20−23] and when compared the specific capacity, rate capability, and Li^+ diffusion ability to those of $TiO_2(B)$ nanorods, it was found that each parameter was greater than other reported titanate-based materials.[15,22−24] Furthermore, raw materials, which were used to improve electrochemical properties in LIBs for synthesizing other titanate materials, such as chromium (Cr),[23,24] strontium (Sr),[25] etc., were rare and more expensive than raw materials of $TiO_2(B)$, which led to a high industrial production cost. In addition, using precious metals (Cr) for synthesizing complex titanate anode materials was more dangerous to humans and organisms than using $TiO_2(B)$ precursors because the metal was harmful to the skin, eyes, blood, and respiratory system, was a human carcinogen[26] and could cause biodiversity loss[27,28] and also environmental pollution.[29] However, the specific capacity of $TiO_2(B)$ is moderate, and the development of electrochemical properties in $TiO_2(B)$ anode materials can be improved by fabricating $TiO_2(B)$ with many composite materials, such as alloying (Si,[30−32] Sn,[33] Sb,[34,35] Ge,[36,37] etc.) and conversion of anode materials (metal oxide,[38−41] metal nitride,[42] metal sulfide,[43,44] etc.). The composite process can increase electrochemical efficiency and retain fast charge property of anode materials in LIBs, as shown in Table S2. Nevertheless, the quality of $TiO_2(B)$ composites is dependent on the types of composite materials and the morphology, phase purity, and crystallinity of $TiO_2(B)$. Therefore, the study of an influence of $TiO_2(B)$ morphology, crystallinity, and phase formation are the key factors to control the electrochemical properties of the composite $TiO_2(B)$.

This research aims to develop $TiO_2(B)$ nanoparticles that were prepared by a hydrothermal process by using the influence of synthesis conditions (temperatures and times) on physical morphology and phase formation to study the electrochemical properties of LIBs. The physical morphology of $TiO_2(B)$ products was characterized by scanning electron microscopy (SEM), and the phase formation was characterized by X-ray diffractometry (XRD). Finally, the characterization of the electrochemical properties of products will be prepared as electrodes and fabricated into coin cells to measure the cycle performance, rate cycle performance, cyclic voltammetry, and electrochemical impedance spectroscopy. We expect that $TiO_2(B)$ nanoparticles in this research will be interested in fabrication composites as high-performance anode materials in EV industrial or other applications in the future because our material has the highest specific capacity compared to other TiO_2 in the literature, as presented in Table S3.

■ MATERIALS AND METHODS

For the synthesis of $TiO_2(B)$ nanoparticles, an anatase titanium dioxide precursor (TiO_2, 98.5%) was purchased from Carlo Erba. Sodium hydroxide (NaOH, 99.5%) was purchased from Merck KGaA, and nitric acid (HNO_3, 65%) was purchased from RCI-Labscan. Deionized water was used as a solvent in reactions.

For fabrication of $TiO_2(B)$ anode materials in 2016-type coin cells to measure the electrochemical properties, Super-P (conductive, carbon black) was purchased from NCM HERSBIT Chemical Co., Ltd. and sodium alginate food grade (binder, SA, 99%) was purchased from Loba Chemie.

Synthesis of $TiO_2(B)$ Nanoparticles via Hydrothermal Method. The preparation of $TiO_2(B)$ nanoparticles consisted of 3 processes: the hydrothermal method, ion exchange, and calcination. First, 1.0 g of powdered Ti precursor was dissolved in 70 mL of 10 M NaOH solution. Then, the suspension was stirred and sonicated at room temperature. After that, the homogeneous mixture was transferred to hydrothermal reactors. And then, the hydrothermal vessel was heated at different temperatures (180 and 220 °C) and reaction times (3, 12, 24, 36, 48, and 120 h). The excess NaOH in the precipitate was washed with deionized water several times until the pH approached 7−8. Next, the precipitate was soaked in 1 M HNO_3 overnight and dried at 80 °C by an ion exchange process. The intermediate product of hydrogen titanate was obtained. Finally, the hydrogen titanate was calcined at 450 °C for 5 hours with a heating rate of 10 °C/min. The final samples of $TiO_2(B)$ were successfully achieved. The samples were named TIOXXX_YY, where XXX and YY correspond to

hydrothermal temperature and hydrothermal time, respectively.

MATERIALS CHARACTERIZATION

Investigation of the phase transformation of the samples was determined by X-ray diffraction (XRD) on a Rigaku Smart Lab SE diffractometer equipped with Cu Kα radiation. Scanning electron microscopy (SEM, JSM-IT800) was operated with gold-coated samples to study the morphology and particle size. Transmission electron microscopy (TEM, JEOL JEM 2010) was used to examine the in-depth microscopy and phase confirmation.

ELECTROCHEMICAL MEASUREMENTS

The TiO$_2$(B) anode materials were fabricated as 2016-type coin cells to study the electrochemical performances. First, the working electrodes were prepared by mixing 70 wt % TiO$_2$(B) sample, 20 wt % conductive Super-P, and 10 wt % SA, binder in DI water to form a homogeneous slurry. Then, the mixed slurry was cast on Cu foil with a thickness of 150 μm. Then, the electrode was dried 2 times. For the first time, the electrode was dried at 80 °C for 24 h. After that, it was dried under a vacuum oven at 80 °C for 24 h. The electrode loading masses were calculated to range from 1.03 to 1.18 mg/cm^2 by eq S1. Next, the prepared electrodes were cut into a circle 13 mm in diameter to be an anode electrode. The coin cell was fabricated in an argon-filled glovebox to avoid moisture and oxygen. The coin cell assembly used a lithium metal chip as the counter electrode. Both sides of the electrodes were separated with a polypropylene (PP, Celgard 2400) membrane as a separator and then soaked with the electrolyte of a 1 M LiPF$_6$ solution in a solution of ethylene carbonate and dimethyl carbonate (EC/DMC, 1:1 v/v). The electrochemical measurements were performed by a Land battery test system (Neware BTS4000) with a fixed cut-off voltage window of 0.01−3.00 V at room temperature. The cycle performance measurement was operated for 100 cycles at a current density of 100 mA/g and for 1000 cycles at a current density of 5000 mA/g. The rate performance was measured at different current densities ranging from 50 to 1000 mA/g. The cyclic voltammetry measurement of the cells was measured at a scan rate of 0.1 mV/s over the range of 0.01−3.0 V at room temperature. Electrochemical impedance spectroscopy (EIS) was measured using a potentiostat/galvanostat (Autolab PGSTAT302N) at room temperature.

RESULTS AND DISCUSSION

The TiO$_2$(B) nanoparticles were synthesized from anatase TiO$_2$ precursor by the hydrothermal process, which was calcined at 450 °C for 5 h. The crystal structure of samples at each synthetic step was evaluated by a powder X-ray diffractometer (XRD). The XRD patterns of samples at hydrothermal temperatures of 180 °C for 3, 12, 24, 36, 48, and 120 h and at hydrothermal temperatures of 220 °C for 12 and 120 h are shown in Figure 1. The TIO180_12, TIO180_24, TIO180_36, TIO180_48, TIO180_120, TIO220_12, and TIO220_120 samples represented the TiO$_2$ mixed phase between the anatase phase (JCPDS 021-1272) and bronze phase (ICDD 01-074-1940). On the other hand, the TiO180_03 matched only the anatase phase (JCPDS 021-1272).
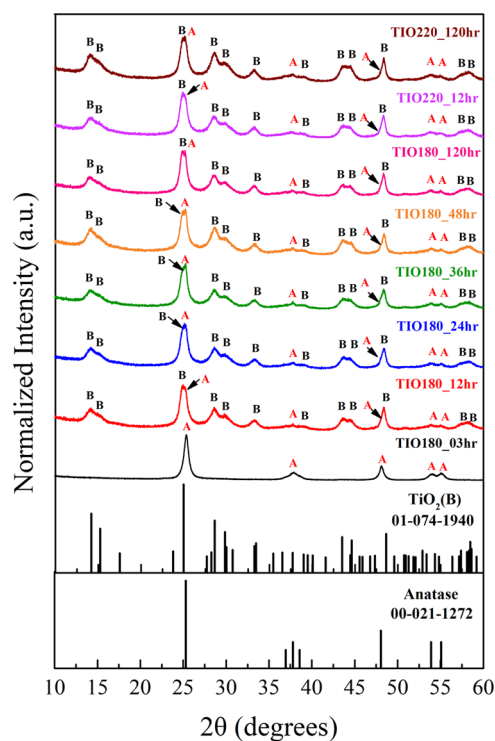
Figure 1. XRD patterns of TiO$_2$ nanoparticles 180 and 220 °C (hydrothermal temperature) at various time periods and calcination 450 °C for 5 h (heating rate 10 °C/min).

We observed that the TiO$_2$(B) phase could occur since the hydrothermal reaction was 180 °C for 12 h. For the influence of hydrothermal times for 3 to 120 h at 180 °C of hydrothermal temperature, we found that the TiO$_2$(B) phase appeared since the hydrothermal time was higher than 12 h, whereas the hydrothermal temperatures and times have no effect on phase change and crystallinity of TIO180_03, TIO180_120, TIO220_12, and TIO220_120.

The change in the crystal structure from the starting anatase TiO$_2$ precursor powder to the one-dimensional TiO$_2$(B) structure, which was synthesized hydrothermally at various hydrothermal temperatures and times, was not significantly affected by the change in proportion between TiO$_2$(B) and anatase. No other peaks were detected in the XRD patterns of the samples.

The SEM results show that the size and morphology of synthesized TiO$_2$ varied at different temperatures and reaction times. The SEM images of TIO180_03, TIO180_12, TIO180_24, TIO180_36, TIO180_48, TIO180_120, TIO220_12, and TIO220_120 samples are shown in Figure 2. Conventionally, the advantage of the hydrothermal process was controlling the size and morphology with high crystallinity.[45] The physical forms of the TiO$_2$ products after hydrothermal synthesis using a high concentration of alkali metal hydroxide solution were one-dimensional morphologies such as wires or rods.

In this study, most samples were elongations of nanorod shape, whereas the particle morphology of TIO180_03 showed nanoparticles and TIO220_120 showed nanowires, as illustrated in Figure 2a−h. The average particle size was manually analyzed from the SEM images using ImageJ software. The average diameters of TIO180_12, TIO180_24, TIO180_36, TIO180_48, TIO180_120, TIO220_12, and
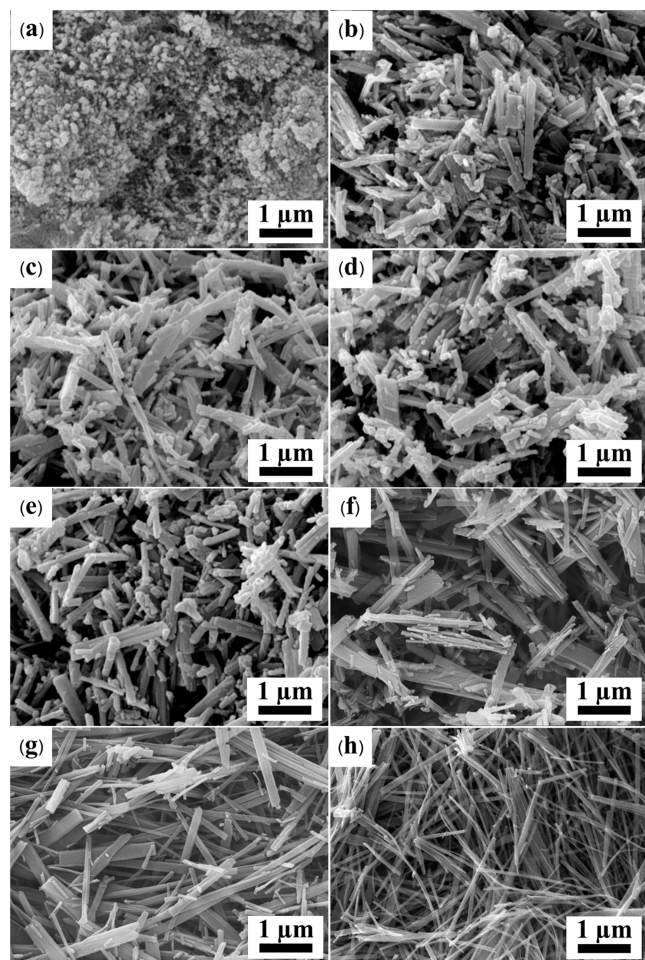
Figure 2. SEM secondary electron images of $TiO_2(B)$ final products from the 6 different hydrothermal times when using a hydrothermal temperature at 180 °C: (a) 3 h, (b) 12 h, (c) 24 h, (d) 36 h, (e) 48 h, and (f) 120 h and a hydrothermal temperature at 220 °C: (g) 12 h and (h) 120 h.

TIO220_120 were 205, 152, 140, 147, 93, 98, and 72 nm, respectively. The average lengths of TIO180_12, TIO180_24, TIO180_36, TIO180_48, TIO180_120, TIO220_12, and TIO220_120 were 926, 1211, 1221, 1251, 1330, 1371, and 1420 nm, respectively. The average particle diameters and lengths of the seven samples were in the same range (in that they were longer than 1 mm). However, TIO180_03 r obviously differed from other samples. In addition, the amount of nucleation and crystal growth was continuously generated during the hydrothermal reaction that caused the transformation of morphology from nanoparticles to nanorods or nanowires with an increase of hydrothermal temperature and reaction time.

ELECTROCHEMICAL MEASUREMENT

The cycling stability of TiO_2 synthesized at 180 and 220 °C hydrothermal temperatures operating at a current density of 100 mA/g within the voltage range of 0.01−3.00 V is shown in Figure 3a. The initial specific capacities of TIO180_03, TIO180_12, TIO180_24, TIO180_36, TIO180_48, TIO180_120, TIO220_12, and TIO220_120 have observed discharge specific capacities of 727.9, 581.6, 564.6, 580.1, 595.2, 601.0, 611.6, and 493.4 mAh/g, respectively, and calculated the initial coulombic efficiencies (ICEs) of 46.7,

60.3, 60.6, 59.5, 60.2, 60.9, 63.9, and 74.9%. The irreversible capacity loss in the 2nd cycle was mainly due to the formation of a solid electrolyte interphase (SEI) layer, which was caused by a reduction of electrolytes on the surface of the electrode. The electrolyte was reported to be able to react with residual H_2O and −OH groups presented on the surface of $TiO_2(B)$.[46] Since the surface of every TiO_2 material synthesized in this work was not protected, the effects became more apparent as the surface area increased. As a result, the material with spherical particle morphology (TIO180_03), which possessed a higher surface area than other nanorod samples, was observed to have less than 50% of its initial coulombic efficiency. In the meantime, $TiO_2(B)$ nanorod materials such as TIO220_12 displayed significantly higher capacity retention. In comparison to formerly published works regarding $TiO_2(B)$-based materials,[1,33] the pure $TiO_2(B)$ nanorod material was found to deliver the first coulombic efficiency of around 60%. This demonstrated that the $TiO_2(B)$ material in this work was an improvement from previous works. Furthermore, the reports from Tang et al. in 2016 about $TiO_2(B)$ arrays (TBNA) revealed the first coulombic efficiency of around 76%.[47] In the following year, the studies about the hierarchical porous flower-like $TiO_2(B)$ anode achieved a coulombic efficiency of 73% in the first cycle.[48] Both results are comparable to the $TiO_2(B)$ material in this work. It was clearly seen that all sample electrodes showed small capacity fading, indicating the good stability of electrodes. At the end of the tests, the reversible capacities of each material decreased to 245.2, 292.1, 288.6, 276.1, 284.4, 306.6, 348.8, and 315.4 mAh/g, respectively, after 100 cycles.

Furthermore, the rate capability was operated with a current density of 50−1000 mA/g, as shown in Figure 3b. The highest specific capacity was observed in the TIO220_12 electrode at each current density, which was higher than the other electrodes in as-synthesized TiO_2 samples. After applying the high current density, the current density in the rate capability measurement was then reversed to conduct at a current density of 50 mA/g, which recovered to a specific capacity of around 337.9 mAh/g. These results indicated that the best reversibility and rate capability were achieved in the TIO220_12 electrode. On the contrary, it was obvious that the TIO180_03 electrodes had the lowest capacity at every current density. After applying a high current density, the specific capacity of this electrode was around 321.6 mAh/g at a current density of 50 mA/g. However, it was found that the specific capacities of TIO180_120 and TIO220_120 were close to TIO220_12 from observation at a high current density. Therefore, the four samples, including TIO180_03, TIO180_120, TIO220_12, and TIO220_120, were selected to perform long-term cycling capability at a high current density.

To evaluate the fast charge ability, high current densities of 5000 mA/g were applied to the TIO180_03, TIO180_120, TIO220_12, and TIO220_120 electrodes for 1000 cycles, as shown in Figure 3c. The capacity retention was recorded at 105.2, 184.2, 207.3, and 155.6 mAh/g. From the observations, the specific capacity of TIO180_03, which was a pure anatase phase, declined, unlike other samples, which were $TiO_2(B)$ phase, which still maintained stability after 1000 cycles. These indicate that the $TiO_2(B)$ electrode had excellent cycling stability in order to be used in the fast charging application. Moreover, TIO220_12, which displayed the best performances, had the most opportunity to be used as a composite $TiO_2(B)$ anode electrode in future LIBs. However, other
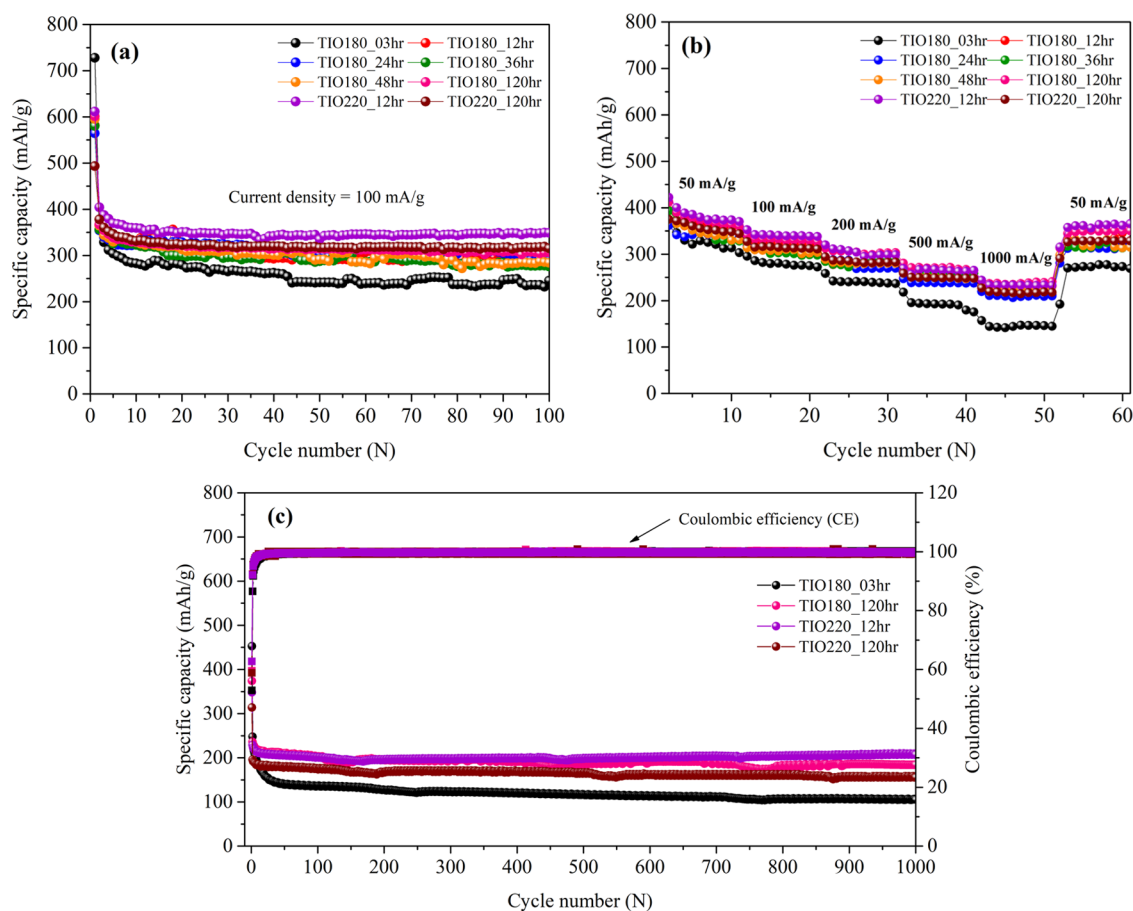
Figure 3. Electrochemical properties of $TiO_2(B)$ nanoparticles: (a) cycle performance at a current density of 100 mA/g for 100 cycles, (b) rate performance at a current density in the range of 50−1000 mA/g, and (c) long-term cycling at a current density of 5000 mA/g.

methods, such as cyclic voltammetry (CV) and electrochemical impedance spectroscopy (EIS) measurements, were needed to confirm the electrochemical properties of each sample.

To comprehend the electrochemical reaction, cyclic voltammograms (CV), as represented in Figure 4, were performed on all synthesized TiO_2: (a) TIO180_03, (b) TIO180_120, (c) TIO220_12, and (d) TIO220_120, with a scan step of 0.1 mV/s between 0.01 and 3.00 V (vs Li/Li$^+$) throughout the first two cycles. In the first two cycles of the typical CV curves of all of the above electrodes, there seemed to be a much larger current pattern in the first discharge stage. This is because electrolyte degradation is needed for the formation of the SEI layer, which forms at the low potential area of all CV curves.[1] In the subsequent cycles, the CV curves were substantially reduced when compared to the first cycle, although major characteristic peaks were still observed and practically overlapped with the first cycle, indicating that the SEI layer predominantly occurred only in the first cycle and that either correlated to specific capacity loss. The electrolyte degradation as a source of the creation of a stable SEI layer mostly on a nanostructured surface may even be essentially summarized as follows (eq (1))[49]

$$Li^+ + e^- + electrolyte \rightarrow SEI(Li) \qquad (1)$$

All of the prepared electrodes showed that they were almost revealed to be characteristic redox peaks of two TiO_2 polymorphs but not in the TIO180_03 electrode (Figure 4a). The reversible capacity of Li$^+$ in the anatase phase, which

matched the combination phase of synthesized TiO_2 found in the XRD patterns, was ascribed to the rather detectable cathodic/anodic peaks at roughly 1.73/1.96 V, which "A" peaks are assigned to the solid-state lithium diffusion in anatase in all CV curves. It is obvious that the peak intensity of anatase in CV curves seems to be quite low in comparison to those other peaks. Because the major diagnostic XRD peaks in nanocrystalline materials with broad diffraction peaks overlap, anatase could be concealed in a combination with a high $TiO_2(B)$ content. Also, the mixture of $TiO_2(B)$ and anatase that is made depends on the recrystallization time, temperature, and titanium substrate. This is a typical result of calcining hydrothermally formed, layered titanates.[9,50,51] Also, $TiO_2(B)$ characteristic peaks, whose "B" peaks are associated with pseudocapacitive lithium storage behavior, performed a potential pair of discharge peaks (intercalation) at 1.49 and 1.55 V and charge peaks (de-intercalation) at 1.58 and 1.64 V.[9] For both phases of TiO_2, a typical reaction mechanism refers to Li-ion interaction with anatase and the $TiO_2(B)$ structure.[52] The initial mechanism for Li-ion insertion and extraction in prepared TiO_2 electrodes can be described by eq 2. In addition, the insertion coefficient (x) is dependent on the polymorphism, morphology, and crystallographic orientation of TiO_2. Typically, x in anatase is equivalent to 0.5.[53] For $TiO_2(B)$, it has previously been stated that the initial discharge of $TiO_2(B)$ could be $Li_xTiO_2(B)$, where x = 0.7−1.0 (with consistent slow rate cycling; meanwhile, x is in the range of
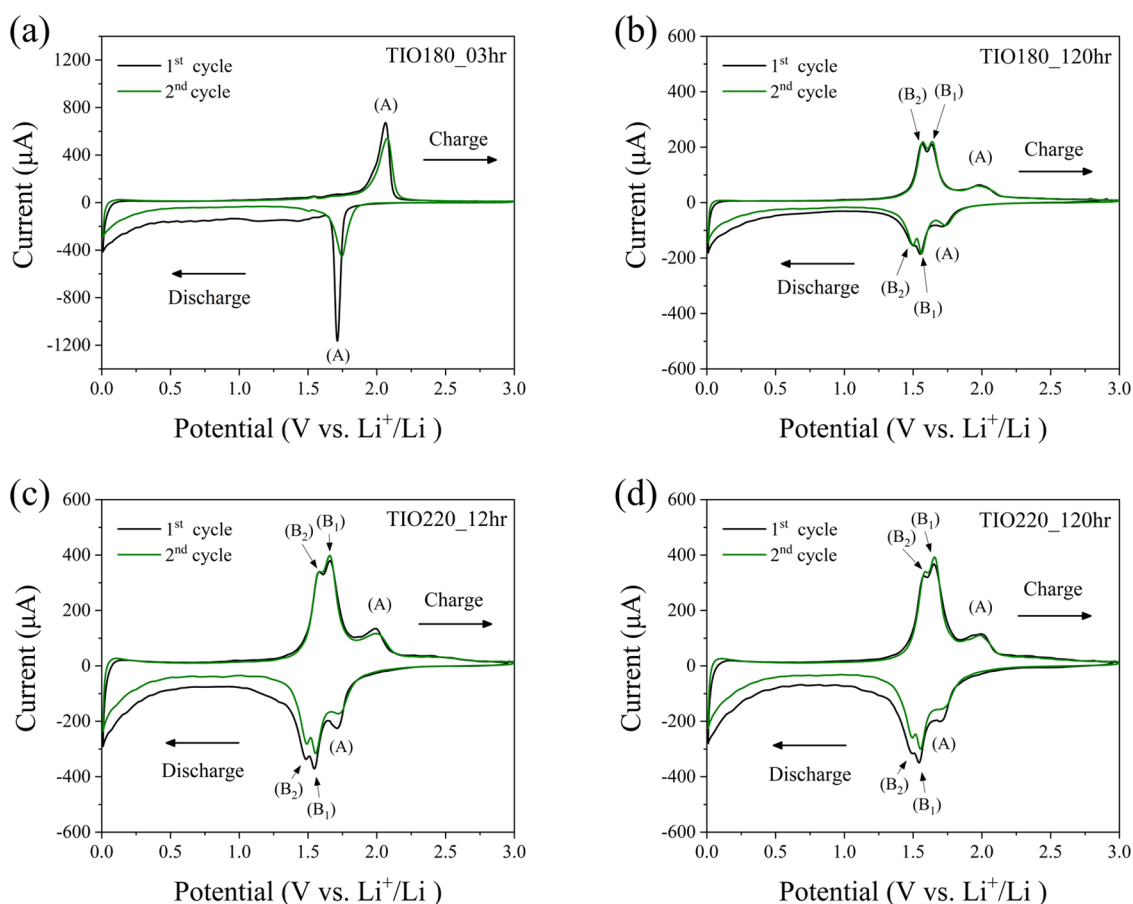
Figure 4. Initial two cyclic voltammograms of prepared TiO$_2$ electrodes showing the 1st (black) and 2nd (green) cycles between voltage cutoffs of 1.0 and 3.0 V at a scan rate of 0.1 mV/s: (a) TIO180_03, (b) TIO180_120, (c) TIO220_12, and (d) TIO220_120.
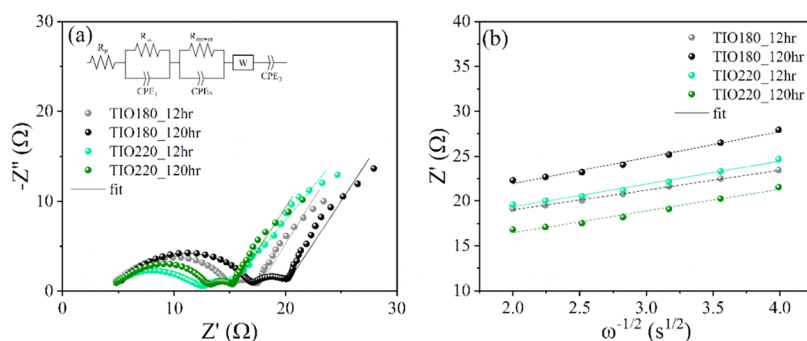

Figure 5. (a) EIS spectra of TiO$_2$ electrodes and (b) relationship between Z' and $\omega^{-1/2}$ from EIS data in the low-frequency region.

Table 1. Fitted Equivalent Circuit Parameters and Calculated Values of Each Material

material	R_p (Ω)	R_∞ (Ω)	R_{ct+mt} (Ω)	σ_p (S/cm)	σ_W ($\Omega/s^{1/2}$)	D_{Li} (cm^2/s)
TIO180_12	4.51	10.7	2.17	3.33×10^{-3}	2.21	3.49×10^{-12}
TIO180_120	5.04	12.07	2.47	2.98×10^{-3}	2.89	2.04×10^{-12}
TIO220_12	3.90	8.83	2.07	3.85×10^{-3}	2.55	2.62×10^{-12}
TIO220_120	4.46	8.80	1.83	3.36×10^{-3}	2.43	2.89×10^{-12}

0.3−0.6).[21,54−56] Li$_x$TiO$_2$(B) is lithiated and delithiated reversibly in repetitive cycles, according to eq 3.

$$TiO_2 + xLi^+ + xe^- \leftrightarrow Li_xTiO_2 \qquad (2)$$

$$Li_xTiO_2(B) \leftrightarrow Li_{x-y}TiO_2(B) + yLi^+ + ye^- \qquad (3)$$
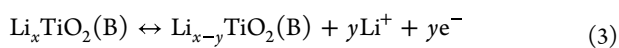
Electrochemical impedance spectroscopy (EIS) was used to observe the electrochemical behavior of each material. Figure 5a displays the EIS spectra of TiO$_2$ materials before a cycle performance test, measured at 0.01−10^5 Hz. These spectra were fitted to a common equivalent circuit model using the Nova 2.1 program, as shown in the inset of Figure 5a. First, a gap between the origin point and the starting point of Nyquist
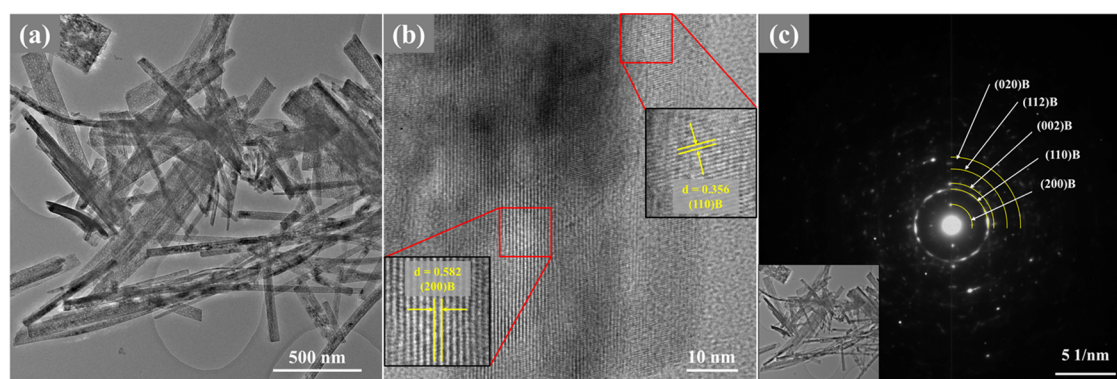
Figure 6. TEM result of the optimal sample (TIO220_12): (a) BF image, (b) HRTEM image, and (c) SAED patterns.

plots indicated the resistance from combined components of the planar electrode (R_p). The relationship between R_p and the conductivity of the electrode material (σ_p) is displayed in the equation below, while L_p represents the thickness of the electrode.

$$R_p = L_p / \sigma_p \tag{4}$$

Next, there were two semicircles within each plot in the high-frequency region. The diameter of the first semicircle usually represented the bulk resistance (R_∞), and the second semicircle were from the charge transfer process between Li and the electrode, along with influences from mass transfer reactions (R_{ct+mt}).[57] The exact values of mentioned parameters were calculated and summarized in Table 1. According to the results, TIO220_12 possessed the lowest overall resistance, followed by TIO220_120, TIO180_12, and TIO180_120. This observation indicated that both temperature and time in the hydrothermal process affected the conductivity of the materials, where the temperature caused more distinctive changes than time. This phenomenon is possibly related to the differences in morphology. As seen in SEM images, TIO220_12 and TIO220_120 possessed more nanorods with a smaller diameter than TIO180_12 and TIO180_120. The presence of these nanorods could increase the electrical contact between materials and conductive carbon, which possibly increase the conductivity. In the meantime, longer hydrothermal times enhanced the length of TiO_2 nanorods, which could enable a longer path for electrons and also result in slightly higher conductivity. This improvement was proven to be beneficial by cycle performance test results (in Figure 3a), where TIO220_12 was able to deliver the most specific capacity compared to other materials.

Lastly, the straight line in the low-frequency region is described by Li$^+$ diffusion into TiO_2 materials, represented by the Warburg element (W).[58] Warburg coefficient (σ_W) can be obtained using the relationship between Z', R, and ω as follows

$$Z' = R + \sigma_w \omega^{-1/2} \tag{5}$$

As shown in Figure 5b, the plots of Z' against $\omega^{-1/2}$ of each sample demonstrated a linear relationship with slopes equal to σ_W.[59] Furthermore, the obtained σ_W was used to calculate the coefficient (D_{Li}) by the following equation

$$D_{Li} = \frac{R^2 T^2}{2n^4 F^4 A^2 C^2 \sigma_W^2} \tag{6}$$

where R is the gas constant, T is the absolute temperature, A is the surface area of the electrode, n is the number of electrons per molecule during oxidization, F is Faraday's constant, C is the concentration of lithium ions, and σ_W is the Warburg coefficient.[60]

The calculated σ_W and D_{Li} are also included in Table 1. Interestingly, TIO180_12 was found to have the highest D_{Li}. Microscopic techniques showed that TIO180_12 consisted of smaller nanorods and nanoparticles than the rest of the samples. These observations also implied that the surface distortion of TIO180_12 was more common, resulting in faster Li diffusion.[18] Nevertheless, the differences in D_{Li} from each material were not significantly distinctive and has not influenced much during cycle performance tests.

All physical characterization results of TiO_2(B) nanoparticles prepared at different conditions showed that hydrothermal temperatures and times had an influence on the morphology, crystallinity, and phase formation of TiO_2(B) particles. The increase in hydrothermal temperature and time caused TiO_2(B) particles to lengthen, forming nanorod and nanowire morphologies. In addition, the higher temperature and time also promote the higher TiO_2(B) crystallinity and lead to a more perfect crystal structure. Therefore, to confirm the phase formation and particle morphology, the optimal sample (TIO220_12) was investigated by bright-field TEM (BF-TEM), high-resolution TEM (HRTEM), and selected area electron diffraction patterns (SAED patterns). The BF-TEM image of TIO220_12 clearly indicated that the particle morphology was solid nanorods, as shown in Figure 6a. The HRTEM image indicated the lattice spacings in single-crystal nanorods of 0.356 and 0.582 nm, respectively, corresponding to the (110) spacing and the (200) spacing of the TiO_2(B) crystal structure, as shown in Figure 6b. Finally, all SAED patterns from a group of the TiO_2(B) nanorods displayed a set of ring spacing characteristic of the TiO_2(B) phase that can be indexed to the (200), (110), (002), (112), and (020) lattice spacings corresponding to XRD patterns, as shown in Figure 6c. To confirm the elemental composition, the optimal sample (TIO220_12) was chosen to clarify the atomic percentage, which was investigated by SEM-EDX analysis. The EDX results suggest the presence of titanium (Ti) and oxygen (O) elements. The atomic ratio (Ti/O) of TIO220_12 was 0.5, corresponding to the theoretical ratio of TiO_2, as shown in Figure S1.

Moreover, the SEM image indicated the morphology of the TIO220_12 anode materials before and after cycling, as shown in Figure S2a,b, respectively. We observed that TiO_2(B)

nanorods before cycling were shortened compared to pristine materials because the anode materials (TiO_2(B), binder, and conductive additives) in the electrode preparation processes were homogenized by grinding and sonication process for a long time. Sonication played an important role in changing the morphology and decreasing the particle size.[61−63] In addition, the morphology of TIO220_12 electrodes after 1000 cycles was covered by a thin SEI layer. There were also no visible cracks on the surface of the electrode, even after 1000 cycles. From the results, it could be concluded that the cycling stability of the optimal TiO_2(B) material was caused by a stable SEI layer, crystallinity, and morphology.

The electrochemical tests represent that the morphology and TiO_2(B) crystallinity are influenced by hydrothermal temperatures and times, which play an important role in specific capacity and rate capability. In addition, the study of long-term cycling stability found that the bronze phase had higher stability than the anatase phase. TiO_2(B) nanorods that were synthesized by using a hydrothermal reaction temperature of 220 °C for 12 h had the highest specific capacity and rate capability because this condition provided an appropriate morphology and high crystallinity for as-synthesized TiO_2(B).

When compared with previous literature, the specific capacity of the optimal material (TIO220_12) was higher than $Li_4Ti_5O_{12}$[15] and other TiO_2[64−70] materials, as well as other carbonaceous materials.[11,12,71,72] However, we found that TIO220_12 was able to maintain excellent stability and possessed a long life cycle compared to carbonaceous materials and titanium oxide-based materials. Moreover, the precursors used to prepare TiO_2(B) nanorods were naturally abundant, nontoxic, environmentally friendly, and low cost. In addition, the synthesis process of TiO_2(B) nanorods is simple, which results in greater economic worthiness compared to the fabrication of other anode materials. Therefore, this material was considered one of the most promising alternative anode materials for sustainable energy storage applications.

CONCLUSIONS

TiO_2(B) nanorods were successfully prepared via a hydrothermal method with a subsequent ion exchange process and calcination. The influences of synthesis conditions such as hydrothermal temperature and hydrothermal time on particle size, particle morphology, and crystallinity of as-synthesized TiO_2(B) were discussed. Moreover, the size of TiO_2(B) nanorods, the crystallinity of the TiO_2(B) structure, and the physical morphology of the TiO_2(B) nanorods have an influence on the battery performance. After 100 cycles, the TiO_2 synthesized at 220 °C hydrothermal temperature for 12 h exhibited the best capacity of 348.8 mAh/g at a current density of 100 mA/g. Also, the optimal TiO_2(B) nanorod materials possessed excellent fast charge ability at 15C and superior cycling stability over 1000 cycles.

ASSOCIATED CONTENT

Ⓢ Supporting Information

The Supporting Information is available free of charge at https://pubs.acs.org/doi/10.1021/acsomega.3c00618.

> It includes an equation for calculating electrode loading masses, three tables of comparison in cycle performance of intercalation anode materials in the lithium-ion battery, a figure of the SEM-EDX quantitative elemental

analysis of the optimal sample electrode, and SEM images of the electrode before and after cycling (PDF)

AUTHOR INFORMATION

Corresponding Author

Yothin Chimupala − *Department of Industrial Chemistry, Faculty of Science, Chiang Mai University, Chiang Mai 50200, Thailand; Center of Excellence in Materials Science and Technology, Chiang Mai University, Chiang Mai 50200, Thailand;* ⓞ orcid.org/0000-0001-5634-2980; Email: yothin.chimupala@cmu.ac.th

Authors

Korawith Pimta − *Department of Industrial Chemistry, Faculty of Science, Chiang Mai University, Chiang Mai 50200, Thailand; Center of Excellence in Materials Science and Technology and Graduate School, Chiang Mai University, Chiang Mai 50200, Thailand*

Thanapat Autthawong − *Department of Chemistry, Faculty of Science and Center of Excellence in Materials Science and Technology, Chiang Mai University, Chiang Mai 50200, Thailand;* ⓞ orcid.org/0000-0001-8023-3864

Waewwow Yodying − *Department of Chemistry, Faculty of Science, Chiang Mai University, Chiang Mai 50200, Thailand*

Chitsanupong Phromma − *Department of Industrial Chemistry, Faculty of Science, Chiang Mai University, Chiang Mai 50200, Thailand*

Mitsutaka Haruta − *Institute for Chemical Research, Kyoto University, Uji 611-0011 Kyoto, Japan;* ⓞ orcid.org/0000-0002-2237-7242

Hiroki Kurata − *Institute for Chemical Research, Kyoto University, Uji 611-0011 Kyoto, Japan;* ⓞ orcid.org/0000-0002-0682-1227

Thapanee Sarakonsri − *Department of Chemistry, Faculty of Science and Center of Excellence in Materials Science and Technology, Chiang Mai University, Chiang Mai 50200, Thailand;* ⓞ orcid.org/0000-0002-3084-0276

Complete contact information is available at:
https://pubs.acs.org/10.1021/acsomega.3c00618

Author Contributions

#K.P. and T.A. are equally contributed as Co-first author.

Notes

The authors declare no competing financial interest.

■ REFERENCES

(1) Autthawong, T.; Yodbunork, C.; Yodying, W.; Boonprachai, R.; Namsar, O.; Yu, A. S.; Chimupala, Y.; Sarakonsri, T. Fast-Charging Anode Materials and Novel Nanocomposite Design of Rice Husk-Derived SiO_2 and Sn Nanoparticles Self-Assembled on $TiO_2(B)$ Nanorods for Lithium-Ion Storage Applications. *ACS Omega* 2022, 7, 1357−1367.

(2) Abraham, K. M. Prospects and Limits of Energy Storage in Batteries. *J. Phys. Chem. Lett.* 2015, 6, 830−844.

(3) Mauger, A.; Xie, H.; Julien, C. M. Composite Anodes for Lithium-Ion Batteries: Status and Trends. *AIMS Mater. Sci.* 2016, 3, 1054−1106.

(4) Tarascon, J.-M.; Armand, M. Issues and Challenges Facing Rechargeable Lithium Batteries. *Nature* 2001, 414, 359−367.

(5) Tavares, C. J.; Vieira, J.; Rebouta, L.; Hungerford, G.; Coutinho, P.; Teixeira, V.; Carneiro, J. O.; Fernandes, A. J. Reactive Sputtering Deposition of Photocatalytic TiO_2 Thin Films on Glass Substrates. *Mater. Sci. Eng.: B* 2007, 138, 139−143.

(6) Madian, M.; Eychmüller, A.; Giebeler, L. Current Advances in TiO_2-Based Nanostructure Electrodes for High Performance Lithium Ion Batteries. *Batteries* 2018, 4, No. 7.

(7) Li, X.; Wu, G.; Liu, X.; Li, W.; Li, M. Orderly Integration of Porous $TiO_2(B)$ Nanosheets into Bunchy Hierarchical Structure for High-Rate and Ultralong-Lifespan Lithium-Ion Batteries. *Nano Energy* 2017, 31, 1−8.

(8) Opra, D. P.; Gnedenkov, Sv.; Sinebryukhov, S. L. Recent Efforts in Design of $TiO_2(B)$ Anodes for High-Rate Lithium-Ion Batteries: A Review. *J. Power Sources* 2019, 442, No. 227225.

(9) Zukalová, M.; Kalbáč, M.; Kavan, L.; Exnar, I.; Graetzel, M. Pseudocapacitive Lithium Storage in $TiO_2(B)$. *Chem. Mater.* 2005, 17, 1248−1255.

(10) Boonprachai, R.; Autthawong, T.; Namsar, O.; Yodbunork, C.; Yodying, W.; Sarakonsri, T. Natural Porous Carbon Derived from Popped Rice as Anode Materials for Lithium-Ion Batteries. *Crystals* 2022, 12, No. 223.

(11) Bhar, M.; Ghosh, S.; Krishnamurthy, S.; Yalamanchili, K.; Martha, S. K. Electrochemical Compatibility of Graphite Anode from Spent Li-Ion Batteries: Recycled via a Greener and Sustainable Approach. *ACS Sustainable Chem. Eng.* 2022, 10, 7515−7525.

(12) Zheng, P.; Liu, T.; Zhang, J.; Zhang, L.; Liu, Y.; Huang, J.; Guo, S. Sweet Potato-Derived Carbon Nanoparticles as Anode for Lithium Ion Battery. *RSC Adv.* 2015, 5, 40737−40741.

(13) Yoo, E.; Kim, J.; Hosono, E.; Zhou, H.; Kudo, T.; Honma, I. Large Reversible Li Storage of Graphene Nanosheet Families for Use in Rechargeable Lithium Ion Batteries. *Nano Lett.* 2008, 8, 2277−2282.

(14) Xu, Y.-T.; Guo, Y.; Li, C.; Zhou, X.-Y.; Tucker, M. C.; Fu, X.-Z.; Sun, R.; Wong, C.-P. Graphene Oxide Nano-Sheets Wrapped Cu_2O Microspheres as Improved Performance Anode Materials for Lithium Ion Batteries. *Nano Energy* 2015, 11, 38−47.

(15) Yi, T.-F.; Xie, Y.; Zhu, Y.-R.; Zhu, R.-S.; Shen, H. Structural and Thermodynamic Stability of $Li_4Ti_5O_{12}$ Anode Material for Lithium-Ion Battery. *J. Power Sources* 2013, 222, 448−454.

(16) Wu, F.; Li, X.; Wang, Z.; Guo, H.; Wu, L.; Xiong, X.; Wang, X. A Novel Method to Synthesize Anatase TiO_2 Nanowires as an Anode Material for Lithium-Ion Batteries. *J. Alloys Compd.* 2011, 509, 3711−3715.

(17) Goriparti, S.; Miele, E.; de Angelis, F.; di Fabrizio, E.; Proietti Zaccaria, R.; Capiglia, C. Review on Recent Progress of Nanostructured Anode Materials for Li-Ion Batteries. *J. Power Sources* 2014, 257, 421−443.

(18) Pham, T. N.; Bui, V. K. H.; Lee, Y.-C. Recent Advances in Hierarchical Anode Designs of TiO_2-B Nanostructures for Lithium-Ion Batteries. *Int. J. Energy Res.* 2021, 45, 17532−17562.

(19) Qi, W.; Shapter, J. G.; Wu, Q.; Yin, T.; Gao, G.; Cui, D. Nanostructured Anode Materials for Lithium-Ion Batteries: Principle, Recent Progress and Future Perspectives. *J. Mater. Chem. A* 2017, 5, 19521−19540.

(20) Lu, J.; Chen, Z.; Pan, F.; Cui, Y.; Amine, K. High-Performance Anode Materials for Rechargeable Lithium-Ion Batteries. *Electrochem. Energy Rev.* 2018, 1, 35−53.

(21) Armstrong, A. R.; Armstrong, G.; Canales, J.; García, R.; Bruce, P. G. Lithium-Ion Intercalation into TiO_2-B Nanowires. *Adv. Mater.* 2005, 17, 862−865.

(22) Yi, T.-F.; Yang, S.-Y.; Xie, Y. Recent Advances of $Li_4Ti_5O_{12}$ as a Promising next Generation Anode Material for High Power Lithium-Ion Batteries. *J. Mater. Chem. A* 2015, 3, 5750−5777.

(23) Yi, T.-F.; Mei, J.; Peng, P.-P.; Luo, S. Facile Synthesis of Polypyrrole-Modified $Li_5Cr_7Ti_6O_{25}$ with Improved Rate Performance as Negative Electrode Material for Li-Ion Batteries. *Composites, Part B* 2019, 167, 566−572.

(24) Wei, T.-T.; Peng, P.; Ji, Y.-R.; Zhu, Y.-R.; Yi, T.-F.; Xie, Y. Rational Construction and Decoration of $Li_5Cr_7Ti_6O_{25}@C$ Nanofibers as Stable Lithium Storage Materials. *J. Energy Chem.* 2022, 71, 400−410.

(25) Dambournet, D.; Belharouak, I.; Amine, K. $MLi_2Ti_6O_{14}$ (M = Sr, Ba, 2Na) Lithium Insertion Titanate Materials: A Comparative Study. *Inorg. Chem.* 2010, 49, 2822−2826.

(26) Jaishankar, M.; Tseten, T.; Anbalagan, N.; Mathew, B.; Beeregowda, K. Toxicity, Mechanism and Health Effects of Some Heavy Metals. *Interdiscip. Toxicol.* 2014, 7, 60−72.

(27) Lee, B.-G.; Wallace, W. G.; Luoma, S. N. Uptake and Loss Kinetics of Cd, Cr and Zn in the Bivalves Potamocorbula Amurensis and Macoma Balthica: Effects of Size and Salinity. *Mar. Ecol.: Prog. Ser.* 1998, 175, 177−189.

(28) Öner, M.; Atli, G.; Canli, M. Changes in Serum Biochemical Parameters of Freshwater Fish Oreochromis Niloticus Following Prolonged Metal (Ag, Cd, Cr, Cu, Zn) Exposures. *Environ. Toxicol. Chem.* 2008, 27, 360−366.

(29) Rodríguez Martín, J. A.; de Arana, C.; Ramos-Miras, J. J.; Gil, C.; Boluda, R. Impact of 70 Years Urban Growth Associated with Heavy Metal Pollution. *Environ. Pollut.* 2015, 196, 156−163.

(30) Ratsameetammajak, N.; Autthawong, T.; Chairuangsri, T.; Kurata, H.; Yu, A.; Sarakonsri, T. Rice Husk-Derived Nano-SiO_2 Assembled on Reduced Graphene Oxide Distributed on Conductive Flexible Polyaniline Frameworks towards High-Performance Lithium-Ion Batteries. *RSC Adv.* 2022, 12, 14621−14630.

(31) Autthawong, T.; Chayasombat, B.; Laokawee, V.; Jarulertwathana, N.; Masuda, T.; Sarakonsri, T. Nanostructural Study of Silicon-Cobalt/Nitrogen-Doped Reduced Graphene Oxide Composites by Electron Microscopy for Using as Anode Material in Lithium-Ion Batteries. *Solid State Phenomena* 2018, 283, 37−45.

(32) Zhou, N.; Wu, Y.; Li, Y.; Yang, J.; Zhou, Q.; Guo, Y.; Xia, M.; Zhou, Z. Interconnected Structure $Si@TiO_2$-B/CNTs Composite Anode Applied for High-Energy Lithium-Ion Batteries. *Appl. Surf. Sci.* 2020, 500, No. 144026.

(33) Autthawong, T.; Yodbunork, C.; Ratsameetammajak, N.; Namsar, O.; Chimupala, Y.; Sarakonsri, T. Enhanced Electrochemical Performance of $Sn(SnO_2)/TiO_2(B)$ Nanocomposite Anode Materials with Ultrafast Charging and Stable Cycling for High-Performance Lithium-Ion Batteries. *ACS Appl. Energy Mater.* 2022, 5, 13829−13842.

(34) Mahamai, N.; Autthawong, T.; YU, A.; Sarakonsri, T. Proportional Effect in SbSi/N-Doped Graphene Nanocomposite Preparation for High-Performance Lithium-Ion Batteries. *Surf. Rev. Lett.* 2021, 28, No. 2150105.

(35) Adpakpang, K.; Sarakonsri, T.; Aifantis, K.; Hackney, S. A. Morphological Study of SnSb/Graphite Composites Influenced by Different Ratio of Sn:Sb. *Rev. Adv. Mater. Sci.* 2012, 32, 12−18.

(36) Autthawong, T.; Promanan, T.; Chayasombat, B.; Yu, A. S.; Uosaki, K.; Yamaguchi, A.; Kurata, H.; Chairuangsri, T.; Sarakonsri, T. Facile Synthesis Sandwich-Structured Ge/NrGO Nanocomposite as Anodes for High-Performance Lithium-Ion Batteries. *Crystals* 2021, *11*, No. 1582.

(37) Kawasaki, M.; Sompetch, K.; Sarakonsri, T.; Shiojiri, M. Scanning Transmission Electron Microscopy Analysis of Ge(O)/ (Graphitic Carbon Nitride) Nanocomposite Powder. *Mater. Charact.* 2015, *110*, 60−67.

(38) Yodying, W.; Sarakonsri, T.; Ratsameetammajak, N.; Khunpakdee, K.; Haruta, M.; Autthawong, T. Low-Cost Production of Fe_3O_4/C Nanocomposite Anodes Derived from Banana Stem Waste Recycling for Sustainable Lithium-Ion Batteries. *Crystals* 2023, *13*, No. 280.

(39) Zhou, Y.; Wang, C.; Chen, F.; Wang, T.; Ni, Y.; Sun, H.; Yu, N.; Geng, B. Synchronous Constructing Ion Channels and Confined Space of Co_3O_4 Anode for High-Performance Lithium-Ion Batteries. *Nano Res.* 2022, *15*, 6192−6199.

(40) Liu, Z.; Yu, M.; Wang, X.; Lai, F.; Wang, C.; Yu, N.; Sun, H.; Geng, B. Sandwich Shelled $TiO_2@Co_3O_4@Co_3O_4$/C Hollow Spheres as Anode Materials for Lithium Ion Batteries. *Chem. Commun.* 2021, *57*, 1786−1789.

(41) Du, H.; Huang, K.; Li, M.; Xia, Y.; Sun, Y.; Yu, M.; Geng, B. Gas Template-Assisted Spray Pyrolysis: A Facile Strategy to Produce Porous Hollow Co_3O_4 with Tunable Porosity for High-Performance Lithium-Ion Battery Anode Materials. *Nano Res.* 2018, *11*, 1490− 1499.

(42) Dong, Y.; Li, Y.; Shi, H.; Qin, J.; Zheng, S.; He, R.; Wu, Z.-S. Graphene Encapsulated Iron Nitrides Confined in 3D Carbon Nanosheet Frameworks for High-Rate Lithium Ion Batteries. *Carbon* 2020, *159*, 213−220.

(43) Deng, H.; Sarakonsri, T.; Huang, T.; Yu, A.; Aifantis, K. Transformation of SnS Nanocomposites to Sn and S Nanoparticles during Lithiation. *Crystals* 2021, *11*, No. 145.

(44) Waket, T.; Sarakonsri, T.; Aifantis, K. E.; Hackney, S. A. Preparation of Tin and Tin Sulfide Alloy on Carbons and Graphene via Chemical Method for Use as Anodes in Lithium-Ion Batteries. *J. Ceram. Process. Res.* 2016, *17*, 73−79.

(45) Hayashi, H.; Hakuta, Y. Hydrothermal Synthesis of Metal Oxide Nanoparticles in Supercritical Water. *Materials* 2010, *3*, 3794− 3817.

(46) Brutti, S.; Gentili, V.; Menard, H.; Scrosati, B.; Bruce, P. G. TiO_2-(B) Nanotubes as Anodes for Lithium Batteries: Origin and Mitigation of Irreversible Capacity. *Adv. Energy Mater.* 2012, *2*, 322− 327.

(47) Tang, Y.; Hong, L.; Wu, Q.; Li, J.; Hou, G.; Cao, H.; Wu, L.; Zheng, G. TiO_2(B) Nanowire Arrays on Ti Foil Substrate as Three-Dimensional Anode for Lithium-Ion Batteries. *Electrochim. Acta* 2016, *195*, 27−33.

(48) Cai, Y.; Wang, H.-E.; Huang, S. Z.; Jin, J.; Wang, C.; Yu, Y.; Li, Y.; Su, B.-L. Hierarchical Nanotube-Constructed Porous TiO_2-B Spheres for High Performance Lithium Ion Batteries. *Sci. Rep.* 2015, *5*, No. 11557.

(49) Chen, J. S.; Archer, L. A.; Wen David Lou, X. SnO_2 Hollow Structures and TiO_2 Nanosheets for Lithium-Ion Batteries. *J. Mater. Chem.* 2011, *21*, 9912−9924.

(50) Chimupala, Y.; Drummond-Brydson, R. Hydrothermal Synthesis and Phase Formation Mechanism of TiO_2(B) Nanorods via Alkali Metal Titanate Phase Transformation. *Solid State Phenomena* 2018, *283*, 23−36.

(51) Chimupala, Y.; Hyett, G.; Simpson, R.; Mitchell, R.; Douthwaite, R.; Milne, S. J.; Brydson, R. D. Synthesis and Characterization of Mixed Phase Anatase TiO_2 and Sodium-Doped TiO_2(B) Thin Films by Low Pressure Chemical Vapour Deposition (LPCVD). *RSC Adv.* 2014, *4*, 48507−48517.

(52) Dylla, A. G.; Henkelman, G.; Stevenson, K. J. Lithium Insertion in Nanostructured TiO_2(B) Architectures. *Acc. Chem. Res.* 2013, *46*, 1104−1112.

(53) Autthawong, T.; Chimupala, Y.; Haruta, M.; Kurata, H.; Kiyomura, T.; Yu, A. S.; Chairuangsri, T.; Sarakonsri, T. Ultrafast-Charging and Long Cycle-Life Anode Materials of TiO_2-Bronze/ Nitrogen-Doped Graphene Nanocomposites for High-Performance Lithium-Ion Batteries. *RSC Adv.* 2020, *10*, 43811−43824.

(54) Zachau-Christiansen, B.; West, K.; Jacobsen, T.; Atlung, S. Lithium Insertion in Different TiO_2 Modifications. *Solid State Ion* 1988, *28*−*30*, 1176−1182.

(55) Zachau-Christiansen, B.; West, K.; Jacobsen, T.; Skaarup, S. Lithium Insertion in Isomorphous MO_2(B) Structures. *Solid State Ion* 1992, *53*−*56*, 364−369.

(56) Inaba, M.; Oba, Y.; Niina, F.; Murota, Y.; Ogino, Y.; Tasaka, A.; Hirota, K. TiO_2(B) as a Promising High Potential Negative Electrode for Large-Size Lithium-Ion Batteries. *J. Power Sources* 2009, *189*, 580−584.

(57) Mei, B.-A.; Lau, J.; Lin, T.; Tolbert, S. H.; Dunn, B. S.; Pilon, L. Physical Interpretations of Electrochemical Impedance Spectroscopy of Redox Active Electrodes for Electrical Energy Storage. *J. Phys. Chem. C* 2018, *122*, 24499−24511.

(58) Choi, W.; Shin, H. C.; Kim, J. M.; Choi, J. Y.; Yoon, W. S. Modeling and Applications of Electrochemical Impedance Spectroscopy (Eis) for Lithium-Ion Batteries. *J. Electrochem. Sci. Technol.* 2020, *11*, 1−13.

(59) Duan, W.; Zhu, Z.; Li, H.; Hu, Z.; Zhang, K.; Cheng, F.; Chen, J. $Na_3V_2(PO_4)_3$@C Core−Shell Nanocomposites for Rechargeable Sodium-Ion Batteries. *J. Mater. Chem. A* 2014, *2*, 8668−8675.

(60) Lin, Q.; Wang, J.; Zhong, Y.; Sunarso, J.; Tadé, M. O.; Li, L.; Shao, Z. High Performance Porous Iron Oxide-Carbon Nanotube Nanocomposite as an Anode Material for Lithium-Ion Batteries. *Electrochim. Acta* 2016, *212*, 179−186.

(61) Raman, V.; Abbas, A. Experimental Investigations on Ultrasound Mediated Particle Breakage. *Ultrason. Sonochem.* 2008, *15*, 55−64.

(62) Jordens, J.; Appermont, T.; Gielen, B.; van Gerven, T.; Braeken, L. Sonofragmentation: Effect of Ultrasound Frequency and Power on Particle Breakage. *Cryst. Growth Des.* 2016, *16*, 6167−6177.

(63) Dai, H.; Wang, T. Y.; Li, M. C. Spotlight on Ultrasonic Fracture Behaviour of Nanowires: Their Size-Dependent Effect and Prospect for Controllable Functional Modification. *RSC Adv.* 2016, *6*, 72080−72085.

(64) Pfanzelt, M.; Kubiak, P.; Fleischhammer, M.; Wohlfahrt-Mehrens, M. TiO_2 Rutile—An Alternative Anode Material for Safe Lithium-Ion Batteries. *J. Power Sources* 2011, *196*, 6815−6821.

(65) Kitchamsetti, N.; Kalubarme, R. S.; Chikate, P. R.; Park, C.-J.; Ma, Y.-R.; Shirage, P. M.; Devan, R. S. An Investigation on the Effect of Li−Ion Cycling on the Vertically Aligned Brookite TiO_2 Nanostructure. *ChemistrySelect* 2019, *4*, 6620−6626.

(66) Ncube, N. M.; Zheng, H. The Effect of Synthesis Temperature on the Properties of TiO_2(B) Nanorods and Its Precursors as Anode Materials for Lithium-Ion Batteries. *Mater. Res. Express* 2020, *7*, No. 015504.

(67) Wang, Y.; Zhang, J. Ultrafine TiO_2(B) Nanowires for Ultrahigh-Rate Lithium-Ion Batteries. *Ionics* 2020, *26*, 1159−1164.

(68) Zhang, W.; Zhang, Y.; Yu, L.; Wu, N.-L.; Huang, H.; Wei, M. TiO_2-B Nanowires via Topological Conversion with Enhanced Lithium-Ion Intercalation Properties. *J. Mater. Chem. A* 2019, *7*, 3842−3847.

(69) Liu, Y.; Guo, M.; Liu, Z.; Wei, Q.; Wei, M. Rapid and Facile Synthesis of Hierarchically Mesoporous TiO_2−B with Enhanced Reversible Capacity and Rate Capability. *J. Mater. Chem. A* 2018, *6*, 1196−1200.

(70) Liu, Y.; Chen, W.; Yang, C.; Wei, Q.; Wei, M. Hierarchical TiO_2-B Composed of Nanosheets with Exposed{010} Facets as a High-Performance Anode for Lithium Ion Batteries. *J. Power Sources* 2018, *392*, 226−231.

(71) Yang, J.; Zhou, X.; Li, J.; Zou, Y.; Tang, J. Study of Nano-Porous Hard Carbons as Anode Materials for Lithium Ion Batteries. *Mater. Chem. Phys.* 2012, *135*, 445−450.

(72) Tao, L.; Huang, Y.; Yang, X.; Zheng, Y.; Liu, C.; Di, M.; Zheng, Z. Flexible Anode Materials for Lithium-Ion Batteries Derived from Waste Biomass-Based Carbon Nanofibers: I. Effect of Carbonization Temperature. *RSC Adv.* **2018**, *8*, 7102−7109.